Exploring the relationship between metal ion valency and electron transfer in copigmentation processes of cyanidin-3-*O*-glucoside in simulated fruit wine solutions

Bo Zhang [a,*], Juan-Di Wu [a], Qiang Wang [b], Shu-Yan Wang [b], Pan-Pan Zhou [b], Li-Ting Han [a]

[a] *Gansu Key Laboratory of Viticulture and Enology, College of Food Science and Engineering, Gansu Agricultural University, Lanzhou, 730070, China*
[b] *College of Chemistry and Chemical Engineering, Lanzhou University, Lanzhou, 730000, China*

ARTICLE INFO

ABSTRACT

In this experiment, five metal ions (K^+, Mg^{2+}, Al^{3+}, Ga^{3+}, and Sn^{4+}) were utilized as copigments to investigate their copigmentation processes with cyanidin-3-*O*-glucoside (C3OG) in simulated fruit wine solutions. The color characteristics were analyzed using Glories and CIELAB methods, and the copigmentation effects were determined spectrophotometrically. Thermodynamic parameters, including the equilibrium constant (K) and standard Gibbs free energy ($\Delta G°$), were calculated to comprehend the binding affinity between metal ions and C3OG. Ultra-fast femtosecond spectroscopy was employed to monitor the photoinduced electron transfer process between C3OG and cations. Theoretical calculations were also conducted to support experimental findings. The results revealed that the presence of metal ions significantly enhanced the color intensity of C3OG in simulated fruit wine solutions. Higher valency cations, particularly Sn^{4+}, Ga^{3+}, and Al^{3+}, exhibited superior copigmentation effects, resulting in significant bathochromic and hyperchromic changes. Thermodynamic analysis confirmed that the interaction between C3OG and metal ions was spontaneous and exothermic. Ultra-fast femtosecond spectroscopy demonstrated that electron transfer from C3OG to metal ions occurred, with the efficiency of transfer being dependent on valency. Theoretical calculations corroborated the experimental results by highlighting the role of metal ions in stabilizing C3OG/metal complexes through electron transfer. The findings presented in this study contribute to a more comprehensive understanding of pigment/metal complexes and the underlying chemistry behind fruit wine color. Furthermore, it advances the theoretical foundation of copigmentation and broadens its applications in the beverage industry.

1. Introduction

The distinctive flavor and sensory characteristics of fruit wine have contributed to its global popularity, establishing it as one of the most appealing beverages worldwide. Various fruits, including grape, lychee, apple, plum, pineapple, banana, and blueberry, have been successfully processed into fruit wines as reported in the literature (Yang et al., 2021). Among these, grape wine stands out as particularly remarkable. However, the color of fruit wine, whether it be grape wine or other types, is a fundamental sensory characteristic that significantly impacts the product's quality and consumer perception. Anthocyanins are the essential pigments in some fruit wines, directly influencing their chromatic characteristics and aging potential through the structural composition and concentration of these compounds. However,

anthocyanins are highly unstable and susceptible to degradation by various factors, such as pH, temperature, oxygen, solvents, and light, leading to changes in color perception (Chen et al., 2024). Therefore, enhancing the stability of anthocyanins has become a crucial focus of fruit wine research.

The phenomenon of copigmentation involves the formation of molecular associations or complexes between anthocyanins and other noncolored copigments, resulting in an increase in absorbance (hyperchromic effect) and, in certain cases, a shift in the maximum absorbance wavelength of the pigment (bathochromic effect) (Wang et al., 2024). Previous studies have demonstrated copigmentation as an environmentally friendly, natural, safe, and practical method for enhancing food coloration while ensuring the stability of anthocyanins and facilitating the production of a wide range of vibrant hues (Huang et al.,

---

2021; Tang et al., 2023; Wardani et al., 2024). Notably, copigmentation not only exerts a positive chromatic impact on young fruit wine but also contributes significantly to the color profile of aged fruit wine (Zhang et al., 2021). Therefore, researchers have paid increasing attention to the copigmentation process, and studies on copigments and their mechanisms have become a popular topic in fruit wine chemistry research.

Different types of compounds, such as alkaloids (Ujihara and Hayashi, 2020), amino acids (Bingol et al., 2022), organic acids (Lv et al., 2022), and polyphenols (Zhao et al., 2020), have been evaluated as copigments in various research studies. Furthermore, the utilization of metal ions has been proposed for the formation of anthocyanin/metal complexes as a type of copigment. These complexes exhibit enhanced chromaticity and intensity compared to pure anthocyanins (Wardani et al., 2024). For example, the study conducted by Fedenko et al. (2017) investigated the interactions between 18 metal ions, such as Cs^+, Mg^{2+}, Ca^{2+}, Mn^{2+}, Zn^{2+}, Cd^{2+}, and Cr^{3+} with anthocyanins. The findings revealed that all cations exhibited a relatively ideal hyperchromic effect. Sigurdson et al. (2017) found that the bathochromic effect resulting from Al^{3+} complexation with anthocyanins was significantly greater than the shift caused by phenolic copigments like *p*-coumaric acid, ferulic acid, and sinapic acid. Moreover, metal ions (*i.e.*, Fe^{2+}/Fe^{3+}) could facilitate the combination of phenolic acids and anthocyanins while enhancing their copigmentation performance (Kunsági-Máté et al., 2008). Furthermore, recent research has confirmed that metal-containing anions (VO_3^-, MoO_4^{2-}, WO_4^{2-}) (Fedenko et al., 2017) along with metal oxide (TiO_2) (Gokilamani et al., 2014) also exhibit excellent copigmentation phenomena when combined with anthocyanins.

Although there have been a certain number of reports on the research of anthocyanin/metal complexes, the underlying copigmentation mechanism remains unclear, and the roles of metal ions are not well-defined. The current understanding is limited to the chelating binding of cations with the *ortho*-dihydroxyl on the B ring of anthocyanins (Cortez et al., 2017) or the assembly of supermolecules like commelinin (Shiono et al., 2005). More in-depth exploration is needed, especially regarding the effects of fruit wines.

With the advancement of modern detection technology, techniques such as UV–Visible spectroscopy, fluorescence spectroscopy, and infrared spectroscopy have become standard tools in copigmentation studies (Zhang et al., 2020). However, due to potential electron transfer processes during copigmentation (Trouillas et al., 2016), these conventional techniques may face challenges such as imprecise tracking of electron transfer pathways, insensitivity to rapid electron transfer processes, and inadequate capture of transient intermediates in reaction processes. Therefore, it is necessary to employ spectroscopic techniques with a high temporal resolution to study the electron transfer behavior of the copigmentation process on an ultrafast time scale. The utilization of ultra-fast femtosecond spectroscopy offers unparalleled advantages in the investigation of the rapid evolution of molecular electronic excited states and the capture of dynamics pertaining to transient intermediates, thereby facilitating a more profound comprehension of the chemical change process (Zhang et al., 2023). For example, using ultra-fast femtosecond spectroscopy, Shen et al. (2022) effectively analyzed the non-radiative pathways and the suppression of radiative transitions in the hydrogen bond electron transfer in the reaction system. Thus, the utilization of ultra-fast femtosecond spectroscopy can yield valuable data for a comprehensive investigation into the copigmentation process and elucidation of its underlying mechanism. Additionally, with the rapid advancement of computer technology, particularly the significant enhancement in high-performance computing capabilities, theoretical calculations can compensate for the limitations of experimental methods (Zhang et al., 2024). They have emerged as crucial tools for investigating material properties and are extensively employed in studying electronic structures and other characteristics of multi-electron systems. For example, the latest publication in *Nature* by Strassfeld and

colleagues successfully elucidated the reaction mechanism through the utilization of theoretical calculations, enabling precise calculations of electronic and free energy variations within the system (Strassfeld et al., 2023).

In this experiment, we selected five metal ions (K^+, Mg^{2+}, Al^{3+}, Ga^{3+}, and Sn^{4+}) commonly found in fruits, such as grapes, apples, and blueberries (some of these metallic elements are often employed as potential dietary supplements and are additionally incorporated during the processing) (Kuang et al., 2022; Shimizu et al., 2022; Squadrone et al., 2020) and employed a simulated fruit wine solution containing cyanidin-3-*O*-glucoside (cyanidin-3-*O*-glucoside is the most common naturally occurring 3-*O*-glycosidic derivative of cyanidin, which is the most widespread anthocyanidin in the plant kingdom) to investigate the copigmentation phenomenon. This study used ultra-fast femtosecond spectroscopy to monitor in situ photoinduced electron transfer processes between anthocyanins and metal ions. The results would provide novel insights into the copigmentation mechanism from a dynamic perspective. Moreover, our objective is to elucidate the intricate mechanism underlying copigmentation between metal cations and anthocyanins by integrating direct dynamic evidence, color characteristics, copigmentation effects, thermodynamic parameters, and theoretical calculation findings while simultaneously expanding its application within the beverage industry.

2. Materials and methods

2.1. Materials

Cyanidin-3-*O*-glucoside (C3OG, purity ≥98%) was purchased from Shanghai Yuanye Biotechnology Co., LTD. (Shanghai, China). Five metal chlorides, namely potassium chloride (KCl), magnesium chloride ($MgCl_2 \cdot 6H_2O$), aluminum chloride ($AlCl_3 \cdot 6H_2O$), gallium chloride ($GaCl_3$), and stannic chloride ($SnCl_4$), were supplied by Shanghai Macklin Biochemical Technology Co., LTD. (Shanghai, China) (purity ≥99%). Distilled water was obtained from Watsons (Guangzhou, China). Unless noted specifically, all other chemicals and solvents were of analytical grade and purchased from Guangfu Chemical Co., LTD. (Tianjin, China) and Shuangshuang Chemical Co., LTD. (Yantai, China).

2.2. Preparation of simulated fruit wine solutions

The simulated fruit wine solution was prepared according to the method of Zhang et al. (2016) with some modifications. The specific preparation process is as follows. The simulated fruit wine solutions contained 5 g/L tartaric acids with 12% (v/v) ethanol. The pH was adjusted to 3.6 by adding a small quantity of NaOH or HCl. The pigment solution was prepared at a concentration twice that of the analysis (0.20 mM) by dissolving C3OG in the simulated fruit wine solution. Similarly, the concentration of the copigment solution in the simulated solution has been adjusted to twice its molar ratio amount (5 mM, 10 mM, 15 mM, and 20 mM) with the pigment/copigment, respectively. Subsequently, the mixture was diluted 1:1 with an aliquot of copigment solution to obtain sample solutions with a pigment/copigment molar ratio of 1:0, 1:25, 1:50, 1:75, and 1:100 at 20 °C. All solutions were prepared in triplicate and equilibrated in the dark for 30 min before analysis.

2.3. Copigmentation and colorimetric measurements

The magnitude of the copigmentation was determined according to the method proposed by Malaj et al. (2013). The visible spectrum (400–700 nm) was recorded at constant intervals ($\Delta\lambda = 1$ nm) with a T9CS UV–Visible spectrophotometer (Beijing General Instruments Co., LTD., Beijing, China), using 2 mm path length glass cells and distilled water as a reference. The hyperchromic shift was calculated as the percentage increase in absorbance at 515 nm, and the bathochromic shift was the change in the maximum absorption wavelength (λ_{max}).

Glories parameters were determined by measuring the absorbance (*A*) values at 420, 520, and 620 nm (Pérez-Magariño & González-San José, 2002). Color intensity (CI = A_{420} + A_{520} + A_{620}), color hue (CH = A_{420}/A_{520}), the proportion of yellow color (Y% = A_{420} × 100/CI), the proportion of red color (R% = A_{520} × 100/CI), and the proportion of blue color (B% = A_{620} × 100/CI) were also calculated.

CIELAB parameters were assessed by measuring the sample transmittance every 1 nm over the visible spectrum, using the D65 illuminant and 10° observer angle (Pérez-Magariño et al., 2002). The color parameters, *L** (lightness), *a** (green/red component), *b** (blue/yellow component), C^*_{ab} (chroma), and h_{ab} (hue), were calculated via the CIE method. Color differences (ΔE^*_{ab}) between two color points in the CIELAB space were determined as the Euclidean distance between their locations in the three-dimensional space, as defined by *L**, *a**, and *b**. Moreover, color swatches were created according to the parameters (*L**, *a**, and *b**) via an online color tool (https://www.colortell.com/colortool).

2.4. Thermodynamic data determination

The equilibrium constant (*K*) and Gibbs free energy ($\Delta G°$) of the copigmentation reaction were determined by formulas (1) – (2).

$$\ln\left(\frac{A - A_0}{A_0}\right) = \ln K + n \ln [CP]_0 \qquad (1)$$

$$\Delta G^0 = -\, RT \times \ln K \qquad (2)$$

Where A_0 is the maximum visible absorbance at $\lambda = 515$ nm for C3OG without metal copigments, and *A* is the absorbance at λ_{515} of C3OG with metal copigments. *K* is the equilibrium constant for the reaction of copigmentation and is defined as $[AH(CP) + n]/([AH^+][CP]^n)$. *n* is the stoichiometric ratio between the anthocyanin and the copigment. $[CP]_0$ represents the concentration of copigment added to the anthocyanin solution. The intercept of the plot of $\ln[(A-A_0)/A_0]$ versus $\ln[CP]_0$ for the copigmentation reaction is expressed as ln*K*. *R* is the gas constant (8.314 J/mol·K), and *T* is the temperature in Kelvin.

2.5. Femtosecond broadband pump-probe spectroscopy measurement

The photoinduced electron transfer process between anthocyanin and metal ions in situ was recorded on a femtosecond broadband pump-probe spectrometer (Legend Elite, Coherent Corp., Pennsylvania, USA). The laser source was a Coherent Legend Elite regenerative amplifier (1 kHz, 800 nm) seeded by a Coherent Chameleon oscillator (75 fs, 80 MHz). The samples were placed in a quartz cuvette with an optical path length of 2 mm and excited at 420 nm. The data fitting was performed by Surface Xplorer software (Falamas et al., 2017).

2.6. Theoretical calculations

Gauss View 6.0 was used to visualize and analyze the structural properties of the molecule. Then, the reactants and products used in this theoretical calculation were first optimized by a semi-empirical method (PM6). In addition, the molecular structure was further optimized to convergence at the level of the Def2TZVP basis (Vaňura et al., 2022) set by the B3LYP-D3 method of density functional theory (DFT) and the zero point energy was corrected. The solvation model chosen was SMD, while the solvent used was a mixed solution with a dielectric constant of 71.8968 F/m. The interaction energy ($\Delta E_{binding}$) for the metal ion/G3OG complexes was calculated via the following equations:

$$\Delta E_{binding} = E_{complex} - E_{C3OG} - E_{metal\ ion} \qquad (3)$$

For formula (3), $E_{complex}$, E_{C3OG}, and $E_{metal\ ion}$ denote the total energy of the complex and the energies of each reactant (Hartree, 1 Hartree = 2625.50 kJ/mol), respectively.

In addition, the energy difference (ΔE) between the highest occupied molecular orbital (HOMO) and the lowest unoccupied molecular orbital (LUMO) can be directly calculated from the energy band structure.

2.7. Statistical analysis

All the experiments were performed in triplicate, and the mean and standard deviation were calculated using Microsoft Excel 2010 (Microsoft, Redmond, WA, USA). One-way analysis of variance (ANOVA) was used to evaluate significant differences ($P \leq 0.05$) between means, followed by multiple comparative analyses using Duncan's test (SPSS 25.0, SPSS Inc., Chicago, IL, USA).

3. Results and discussion

3.1. Color characteristics analysis

The alteration in color is the most prominent manifestation of copigmentation; therefore, our initial investigation focused on the chromatic evolution of metal ion/C3OG complexes. The results presented in Table 1 demonstrate a concentration-dependent trend in the color intensity (CI) of the simulated fruit wine solution, with an incremental increase observed as ion concentrations rise. Additionally, there is a notable correlation between the CI value and the valence state of cations. For example, the Sn^{4+} treatment (at a molar ratio of 1:100) exhibited a significant increase in CI by 280.9% compared to the control sample, surpassing additions of Ga^{3+}, Al^{3+}, Mg^{2+}, and K^+ by factors of 0.67, 1.75, 2.64, and 2.74 times, respectively. The ΔL^* demonstrates that the introduction of metal ions leads to a reduction in solution lightness, with high-valence metal ions exerting a significant influence compared to low-valence ones (−13.97–20.06 a.u. for Sn^{4+}; −4.45–11.09 a.u. for Ga^{3+}; −0.94–3.22 a.u. for Al^{3+}; −0.20–0.49 a.u. for Mg^{2+}; −0.11–0.14 a.u. for K^+, Table 1). Similar trends were also observed in chroma difference (ΔC^*_{ab}) and color hue (CH) results. For example, upon treatment with Sn^{4+}, Ga^{3+}, Al^{3+}, Mg^{2+}, and K^+ at a molar ratio of 1:100, the ΔC^*_{ab} values increased by 38.45, 12.07, 3.39, 1.06, 0.07 a.u., respectively. The addition of Sn^{4+}, Ga^{3+} and Al^{3+} significantly decreased the solution CH levels compared to the untreated sample (decrease of 41.2–47.6%, 9.1–16.2% and 0.9–7.6% at the molar ratio from 1:0 to 1:100, respectively; $P < 0.05$). However, the decrease in CH was less pronounced for Mg^{2+} treatment (0.005–0.014 a.u.), while K^+ addition did not result in significant changes in CH value ($P > 0.05$).

In color analysis, the hue of a sample can also be further examined by analyzing changes in yellow, red, and blue colors (Zeece, 2020). The proportions of yellow (Y%), red (R%), and blue (B%) colors after different cation treatments were observed to follow the order R% > Y% > B%, as indicated in Table S1 of the Supplementary material. In particular, the simulated fruit wine solutions treated with Sn^{4+}, Ga^{3+}, and Al^{3+} exhibited a significant decrease in Y% and an increase in R% and B%. In accordance with the principles of additive color mixing, the combination of yellow, red, and blue can generate a wide range of colors. For example, red and blue elements can be mixed to form a purple color (Zeece, 2020). The R%+B% values increased in the simulated fruit wine solution after treatment with Sn^{4+}, Ga^{3+}, and Al^{3+} (at molar ratios from 1:0 to 1:100), with ranges of 74.1–85.0%, 74.1–81.9%, and 74.1–78.4%, respectively, indicating an enhancement in the intensity of red and blue colors as well as the development of purple features (Fig. 1a–e). As expected, a similar result was found in the CIELAB system. The Δa^* values of the solutions treated with Sn^{4+}, Ga^{3+}, and Al^{3+} exceeded 0.00 a.u., while the Δb^* values were significantly lower than 0.00 a.u. (Table 1). Therefore, the addition of metal ions, specifically Sn^{4+}, Ga^{3+}, and Al^{3+}, significantly enhanced the red and blue attributes of the samples in comparison to the simulated fruit wine solution without these cation treatments. For example, the Δa^* values increased by 8.90, 4.81, and 2.24 a.u., respectively ($P < 0.05$), as ion concentrations rose from 1:0 to 1:100; meanwhile, the Δb^* values

Table 1

Color parameters (CI, CH, ΔL^*, Δa^*, Δb^*, ΔC^*_{ab}, and Δh^*) of copigmentation between five metal ions and C3OG at different molar ratios.

Color parameters	Metal ions	Molar ratios [a, b]				
		1:0	1:25	1:50	1:75	1:100
CI	K^+	0.173β a±0.000	0.174αβ d±0.000	0.175αβ d±0.000	0.176αβ d±0.000	0.176αβ d±0.001
	Mg^{2+}	0.173γ a±0.001	0.174γ d±0.002	0.177β d±0.000	0.178β d±0.001	0.181α d±0.001
	Al^{3+}	0.173ε a±0.002	0.192δ c±0.002	0.208γ c±0.002	0.221β c±0.001	0.240α c±0.003
	Ga^{3+}	0.173ε a±0.001	0.258δ b±0.001	0.314γ b±0.002	0.358β b±0.001	0.394α b±0.001
	Sn^{4+}	0.173ε a±0.000	0.489δ a±0.002	0.587γ a±0.001	0.630β a±0.001	0.659α a±0.003
CH	K^+	0.340β a±0.000	0.349αβ a±0.001	0.350αβ a±0.004	0.345αβ a±0.004	0.347αβ a±0.002
	Mg^{2+}	0.340α a±0.000	0.335αβ b±0.005	0.328βγ b±0.001	0.331βγ b±0.003	0.326γ b±0.003
	Al^{3+}	0.340α a±0.000	0.337β b±0.000	0.324γ b±0.005	0.314γ c±0.004	0.314γ c±0.004
	Ga^{3+}	0.340α a±0.000	0.309β c±0.001	0.294γ c±0.002	0.286δ d±0.002	0.285δ d±0.003
	Sn^{4+}	0.340α a±0.000	0.200β d±0.001	0.184γ d±0.001	0.180δ e±0.001	0.178δ e±0.001
ΔL^*	K^+		−0.11α a±0.08	−0.09α a±0.04	−0.14α a±0.02	−0.14α a±0.02
	Mg^{2+}		−0.20α b±0.07	−0.36β b±0.04	−0.34β b±0.02	−0.49γ b±0.03
	Al^{3+}		−0.94α c±0.06	−1.72β c±0.04	−2.40γ c±0.05	−3.22δ c±0.04
	Ga^{3+}		−4.45α d±0.06	−7.24β d±0.04	−9.40γ d±0.03	−11.09δ d±0.05
	Sn^{4+}		−13.97α e±0.12	−17.47β e±0.06	−19.12γ e±0.08	−20.06δ e±0.12
Δa^*	K^+		0.12α e±0.07	0.11α e±0.05	0.19α e±0.10	0.07α e±0.06
	Mg^{2+}		0.37γ d±0.05	0.74β d±0.11	0.83β d±0.08	1.06α d±0.05
	Al^{3+}		0.71δ c±0.05	1.45γ c±0.02	2.17β c±0.01	2.95α c±0.02
	Ga^{3+}		2.94δ b±0.16	4.95γ b±0.09	6.50β b±0.12	7.75α b±0.16
	Sn^{4+}		23.37δ a±0.16	28.72γ a±0.13	30.92β a±0.20	32.27α a±0.06
Δb^*	K^+		0.05α a±0.02	0.09α a±0.04	0.06α a±0.04	0.06α a±0.02
	Mg^{2+}		−0.09α b±0.04	−0.13α b±0.08	−0.09α b±0.10	−0.09α b±0.04
	Al^{3+}		−1.03α c±0.05	−1.83β c±0.10	−2.58γ c±0.06	−3.32δ c±0.06
	Ga^{3+}		−5.48α d±0.10	−8.80β d±0.07	−11.43γ d±0.10	−13.39δ d±0.14
	Sn^{4+}		−16.08α e±0.18	−20.46β e±0.08	−22.54γ e±0.18	−23.69δ e±0.14
ΔC^*_{ab}	K^+		0.12α e±0.08	0.11α e±0.04	0.18α e±0.01	0.07α e±0.02
	Mg^{2+}		0.37γ d±0.05	0.74β d±0.12	0.83β d±0.08	1.06α d±0.05
	Al^{3+}		0.78δ c±0.05	1.62γ c±0.01	2.46β c±0.03	3.39α c±0.03
	Ga^{3+}		4.04δ b±0.16	7.26γ b±0.05	9.94β b±0.12	12.07α b±0.17
	Sn^{4+}		27.07δ a±0.19	33.80γ a±0.14	36.72β a±0.25	38.45α a±0.08
Δh^*	K^+		0.27α a±0.46	0.45α a±0.17	0.32α a±0.15	0.22α a±0.02
	Mg^{2+}		−0.46α b±0.15	−0.43α b±0.28	−0.27α b±0.37	−0.19α b±0.16
	Al^{3+}		−4.56α c±0.23	−7.60β c±0.43	−10.09γ c±0.21	−12.20δ c±0.20
	Ga^{3+}		−19.68α d±0.35	−26.74β d±0.12	−30.86γ d±0.39	−33.20δ d±0.44
	Sn^{4+}		−22.36α e±0.29	−24.47β e±0.24	−25.46γ e±0.20	−25.89γ e±0.28

Note.

[a] · The distinct letter superscripts within the same row indicate statistically significant differences in the sample at different molar ratios ($P < 0.05$). The distinct letter subscripts within the same column signify a significant distinction among differently treated samples ($P < 0.05$).

[b] The unit of data in the table is a.u.

decreased by 7.61, 7.91, and 2.29 a.u., respectively ($P < 0.05$). However, no significant changes were observed in the Glories (R%+B% = 74.1–75.7%) and CIELAB parameters ($\Delta a^* = 0.07$–0.12 a.u., $\Delta b^* = 0.05$–0.09 a.u.) for K^+ ($P > 0.05$).

The color difference (ΔE^*_{ab}) was calculated between the simulated fruit wine solutions in the absence and presence of metal cations. Considering $\Delta E^*_{ab} \geq 3$ a.u. reflects differences in red wine colors that are easily discriminated by the human eye (Martínez et al., 2001), the greatest ΔE^*_{ab} values were observed in the solutions containing Sn^{4+}, followed by Ga^{3+} and Al^{3+} (Fig. 1f), with these values significantly exceeding 3 a.u. For example, the Sn^{4+} treatments showed a significant color change (31.62 a.u.) at a molar ratio of 1:25. The ΔE^*_{ab} of Ga^{3+} was 7.65 a.u. (at a molar ratio of 1:25), while adding Al^{3+} led to discernible variations in color (4.13 a.u.) at higher concentrations, such as 1:75. In contrast, Mg^{2+} treatment only yielded a ΔE^*_{ab} of 1.17 a.u., even at its highest ion concentration (1:100). Similarly, K^+ treatment showed minimal perceptible changes to the simulated solution's color difference, with ΔE^*_{ab} ranging from 0.17 to 0.25 au., at molar ratios from 1:0 to 1:100, respectively. The chromatic effect mentioned above demonstrates that each of the five tested metal ions exhibits distinct copigmentation differences, thus necessitating thorough analysis and comparison of their copigmentation effects.

3.2. Copigmentation effects analysis

In general, copigmentation effects are characterized by hyperchromic ($\Delta A\%$) and bathochromic ($\Delta \lambda$) shifts (Boulton, 2001). As illustrated in Fig. 2, the visible spectra of the simulated fruit wine solutions treated with different metal ions displayed variations. The enhancements in both hyperchromic and bathochromic shifts ($\Delta A\% = 1.1$–258.2%, $\Delta \lambda = 0$–33 nm; Table S2) were observed for solutions containing Mg^{2+}, Al^{3+}, Ga^{3+}, and Sn^{4+} as the ion concentration increased (from 1:0 to 1:100), indicating that higher levels of copigments generally lead to more pronounced effects on copigmentation (Zhang et al., 2016). This finding is consistent with our observed color changes. However, with the addition of K^+, the visible spectra of the solution did not change much with increasing ion concentration ($P > 0.05$). Even at the highest molar ratio (1:100), the absorbance and maximum absorption wavelength of the K^+-treated sample remained virtually indistinguishable from those of the control counterpart (0.131 a.u. and 515 nm in K^+-addition samples *vs.* 0.129 a.u., 515 nm in control counterpart). Czibulya et al. (2015) previously reported that the presence of potassium ions enhanced the color of red wine and induced a copigmentation phenomenon, which may be attributed to the types of pigments and reaction conditions employed in different systems (Boulton, 2001; Trouillas et al., 2016).

Among the various metal cations, tetravalent Sn^{4+} demonstrated superior copigmentation performance, exhibiting significant hyperchromic effects ranging from 169.5 to 258.2% ($P < 0.05$) and bathochromic shifts of 12–30 nm ($P < 0.05$) at molar ratios from 1:0 to 1:100 (Fig. 2 and Table S2). Similarly, trivalent Ga^{3+} and Al^{3+} also served as effective copigments, exhibiting a significant 83.7% (Ga^{3+}) and 29.2% (Al^{3+}) enhancement in hyperchromic effects, accompanied by bathochromic shifts by 33 nm (Ga^{3+}) and 7 nm (Al^{3+}) at a molar ratio of
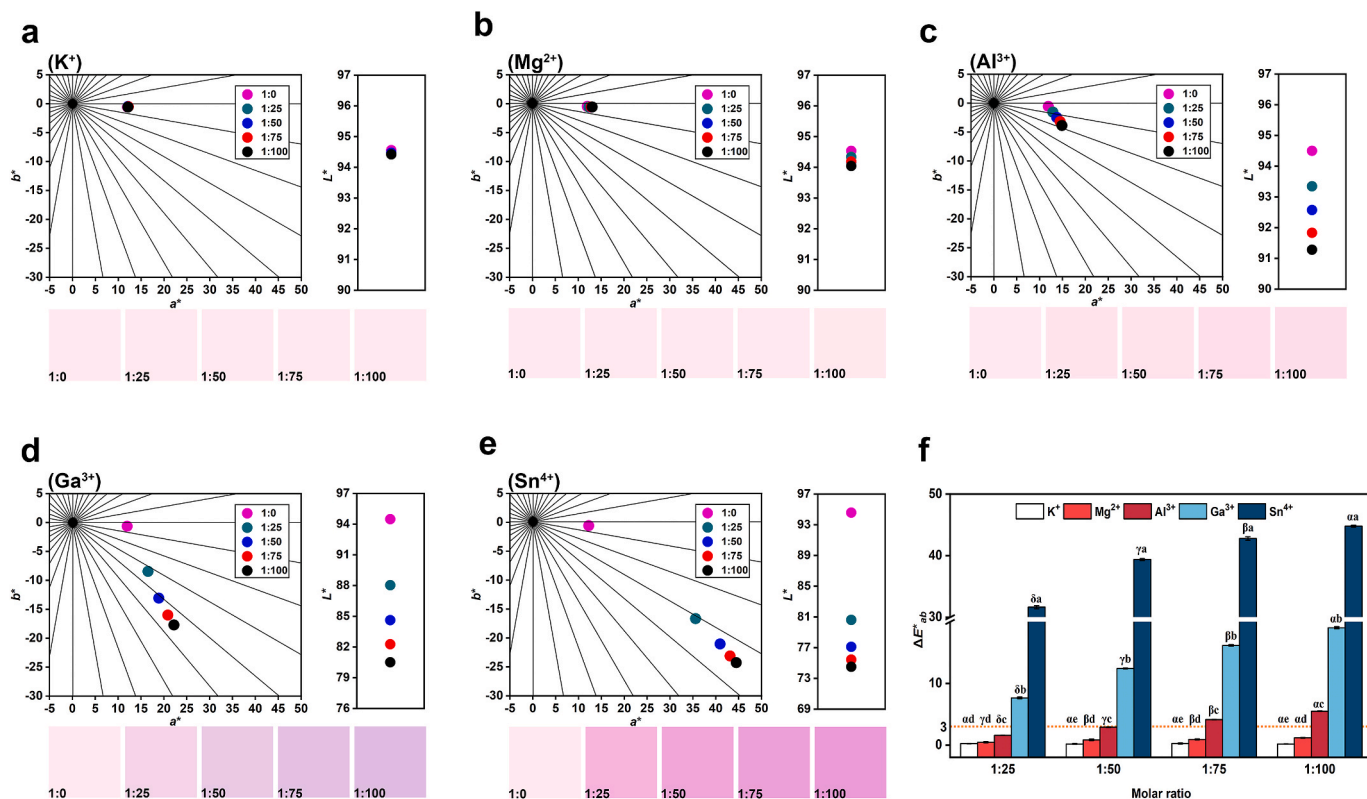
Fig. 1. CIELAB color space ($a*b*$) – plane and lightness ($L*$), and visualization color of five metal ion/C3OG complexes (a–e); $\Delta E*_{ab}$ of copigmentation of different metal-copigment complexes at different molar ratios (f; *Note*: The letters a–e indicate that different metal ions differ at the same concentration, $P < 0.05$; and the letters α–δ indicate that the same metal ion differs at different concentrations, $P < 0.05$. (For interpretation of the references to color in this figure legend, the reader is referred to the Web version of this article.)
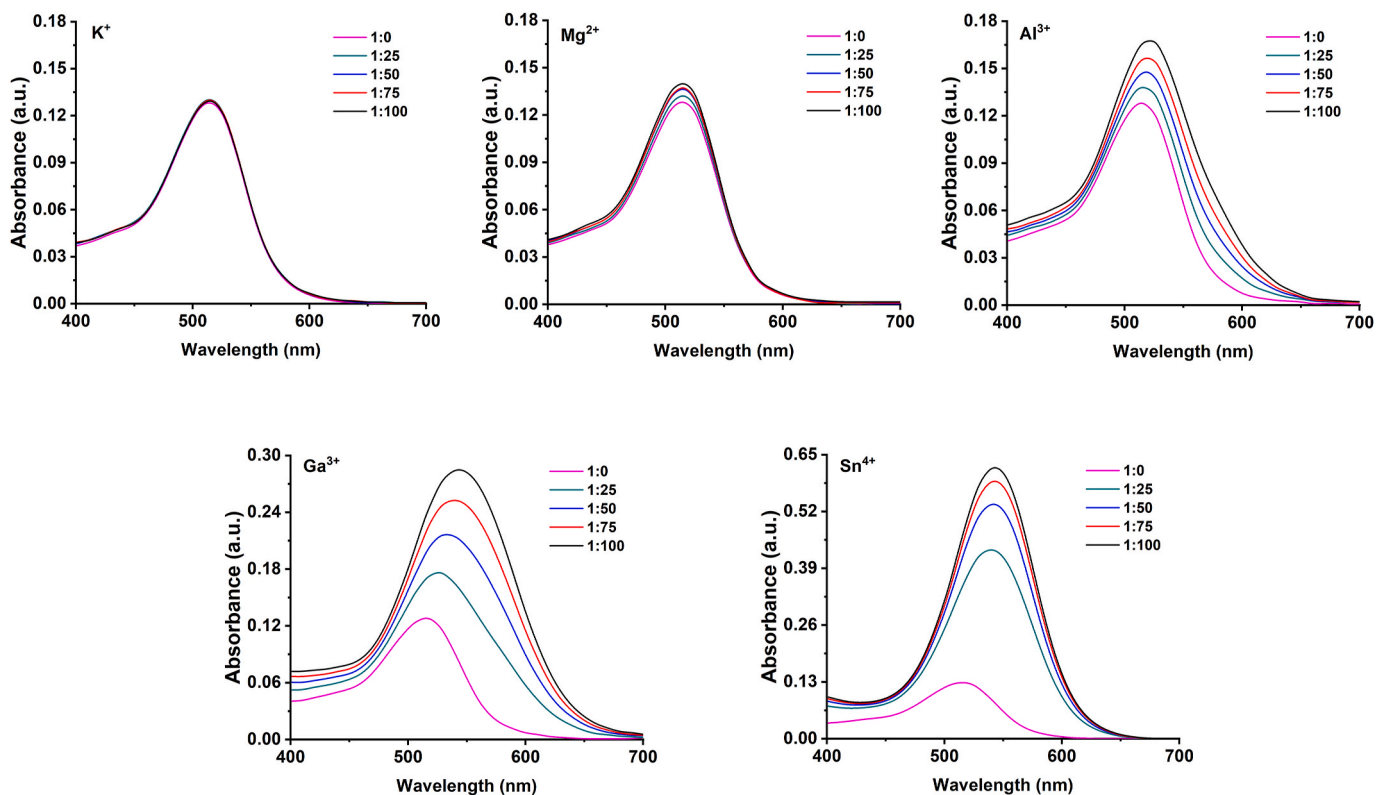

Fig. 2. Visible spectra of copigmentation between five metal ions and C3OG at different molar ratios.

1:100 with C3OG, respectively. In contrast, the copigmentation effect of divalent Mg^{2+} and monovalent K^+ with C3OG exhibited a relatively weaker impact on color intensity enhancement, resulting in only minor improvements ranging from 1.1% to 6.5%, without any observed shifts towards longer wavelengths. These findings suggest that the valence state of cations positively correlates with their copigmentation effect, following the trend $Sn^{4+} > Ga^{3+} > Al^{3+} > Mg^{2+} > K^+$. The reaction between metal ions and anthocyanins of purple sweet potato yielded a similar trend (Li et al., 2016). For example, the researchers observed that the hyperchromic effect of cations followed a descending order: $Al^{3+}Fe^{2+}Cu^{2+}Zn^{2+}Mg^{2+}Ca^{2+}K^+$. The suggestion has been made that the stability of anthocyanin copigment complexes could be significantly enhanced by electron transfer occurring between anthocyanins and copigments (Ferreira da Silva et al., 2005). As good electron transport candidates, the valence state of metal cations directly impacts the rate of electron transport (Gal, 2011). Therefore, the observed variation in the copigmentation effect in our experiment may be attributed to this factor (Estévez et al., 2010). Nevertheless, a more comprehensive investigation is required to thoroughly analyze the performance of copigmentation and elucidate its underlying mechanism.

3.3. Thermodynamic parameters analysis

Thermodynamic experiments can be conducted to elucidate the copigmentation mechanism, with the equilibrium constant (K) serving as a key index reflecting the binding capacity between copigments and anthocyanins. A higher value of K indicates stronger associations (Trouillas et al., 2016). As shown in Table 2, Al^{3+} exhibited a greater affinity for C3OG ($K = 24.43$ L/mol), followed by Mg^{2+} (3.11 L/mol) and K^+ (0.0043 L/mol), which is consistent with the trend of the copigmentation effect discussed above. However, for Sn^{4+} and Ga^{3+}, which exhibited excellent copigmentation effects, the K values were found to be lower than that of Al^{3+} (24.43 L/mol in Al^{3+} *vs.* 10.83 L/mol in Sn^{4+} and 20.87 L/mol in Ga^{3+}), thereby indicating a discrepancy between their K values and the observed copigmentation effect. Previous studies have revealed that Al^{3+}, Ga^{3+}, Sn^{4+}, Mg^{2+}, and K^+ ionic radii are 0.54, 0.62, 0.69, 0.72, and 1.38 Å, respectively (Li, 2020). From this perspective, it is hypothesized that metal ions with larger radii, when combined with C3OG, may exhibit steric hindrance effects that hinder their association with anthocyanins. The smaller n values of Ga^{3+} (0.70) and Sn^{4+} (0.31) can also indirectly support this hypothesis by suggesting a lower ratio of copigment to anthocyanin combination. Therefore, the restriction imposed by the larger ion radius is presumably one of the contributing factors for the lower K value of Sn^{4+} and Ga^{3+} compared to Al^{3+}. However, it is noteworthy that both Sn^{4+} (1.96 eV) and Ga^{3+} (1.81 eV) exhibit higher electronegativity values than Al^{3+} (1.61 eV), Mg^{2+} (1.31 eV), and K^+ (0.82 eV) (Li, 2020). The steric hindrance resulting from their respective ionic radii may not significantly affect their electron-accepting ability from anthocyanins. In contrast, the higher electronegativity of Sn^{4+} and Ga^{3+} compared to Al^{3+} enhances their capabilities in accepting and transferring electrons, thereby facilitating efficient electron flow between the B ring of anthocyanins and the metal

ions. This process could lead to notable color changes in the solution (Zeece, 2020). As a result, Sn^{4+} and Ga^{3+} exhibited better copigmentation effects and color expression than Al^{3+}.

The standard Gibbs free energy ΔG° of the reaction can be determined using the equation $\Delta G^\circ = -RT \times \ln K$. All metal cations, except for K^+, displayed negative ΔG° values (<0 kJ/mol) (Table 2), indicating a spontaneous and exothermic interaction (Zhang et al., 2020). Furthermore, theoretical investigations were carried out to gain a comprehensive understanding of the experimental data. The calculated binding energy ($\Delta E_{binding}$) of the cation/C3OG complexes showed similar trends to the experimental ΔG° (Table 2), reaffirming the interaction between the metal cation and C3OG. Following energy optimization, Fig. 3 illustrates the spatial configurations of the cation/C3OG complex. The optimized spatial arrangement indicates that metal ions are predominantly situated in close proximity to the B ring of C3OG, which aligns with Schreiber's findings (Schreiber et al., 2010). It was observed that these metal ions compete with hydrogen ions attached to the B ring, resulting in complex formation. The charge density diagram demonstrated the overlapping electron densities of reactant atoms, thereby providing support for our hypothesis regarding the occurrence of electron transfer between metal ions and anthocyanins. Moreover, the variation in electron density clouds among Sn^{4+}, Ga^{3+}, Al^{3+}, Mg^{2+}, and K^+ complexes further emphasizes the correlation between ion valence state and copigmentation effect (Fig. 3). However, a more comprehensive analysis is required to delve deeper into this outcome.

3.4. Ultra-fast electron transfer process analysis

Femtosecond transient absorption (TA) spectroscopy is a powerful tool to reveal the ultra-fast dynamics of excited states in materials upon photoexcitation. It has been extensively employed to investigate charge/energy transfer processes in various fields, including (artificial) photosynthesis, photocatalysis, solar cells, and biological systems (Zhai et al., 2020). In this study, we employed this cutting-edge technology to investigate the photoinduced ultra-fast dynamics of anthocyanin. The time-wavelength-intensity 3D spectra of C3OG and its complexes with representative metal ions Mg^{2+} and Sn^{4+} are presented in Fig. 4a–c, along with the extracted dynamic curves shown in Fig. S2. Notably, negative bands centered around 525 nm were clearly observed within the ~450–550 nm range. The observed bands were attributed to anthocyanin's photoinduced bleaching (PB). Upon complexation with Mg^{2+}, the Mg^{2+}/C3OG complex exhibited a similar PB band shape (Fig. 4b and e). However, in the case of the Sn^{4+}/C3OG complex, the PB band displayed a broader range, extending up to 600 nm, with a peak shift to 550 nm (Fig. 4c and f), which is consistent with the steady-state absorption spectra and indicative of the influence exerted by higher valent metal ions.

We then conducted quantitative analysis by fitting the dynamic curves of anthocyanin and its complexes. Fig. 4g illustrates the kinetic trace of anthocyanin at 525 nm under 420 nm excitation, which can be fitted with two components: a short lifetime component ($\tau 1$) of 3.5 ps and a long lifetime component ($\tau 2$) of 146.0 ps, resulting in an averaged

Table 2
Thermodynamic properties of the copigmentation processes between five metal ions and C3OG at different molar ratios [a].

Complex	Experimental [a]			Theoretical [b]			
	n	K (L/mol)	ΔG° (kJ/mol)	$E_{complex}$ (Hartree)	E_{C3OG} (Hartree)	$E_{metal\ ion}$ (Hartree)	$\Delta E_{binding}$ (Hartree)
K^+/C3OG	0.84	0.0043	13.28	−2238.14	−1638.35	−599.76	−0.0261
Mg^{2+}/C3OG	0.76	3.11	−2.76	−1838.13	−1638.35	−199.75	−0.0347
Al^{3+}/C3OG	0.97	24.43	−7.79	−1880.04	−1638.35	−241.33	−0.4032
Ga^{3+}/C3OG	0.70	20.87	−7.40	−3562.36	−1638.35	−1923.74	−0.3073
Sn^{4+}/C3OG	0.31	10.83	−5.80	−1852.28	−1638.35	−213.89	−0.0762

Note.
[a] ΔG° is determined by formula (2): $\Delta G^\circ = -RT \times \ln K$, T = 293.15 K.
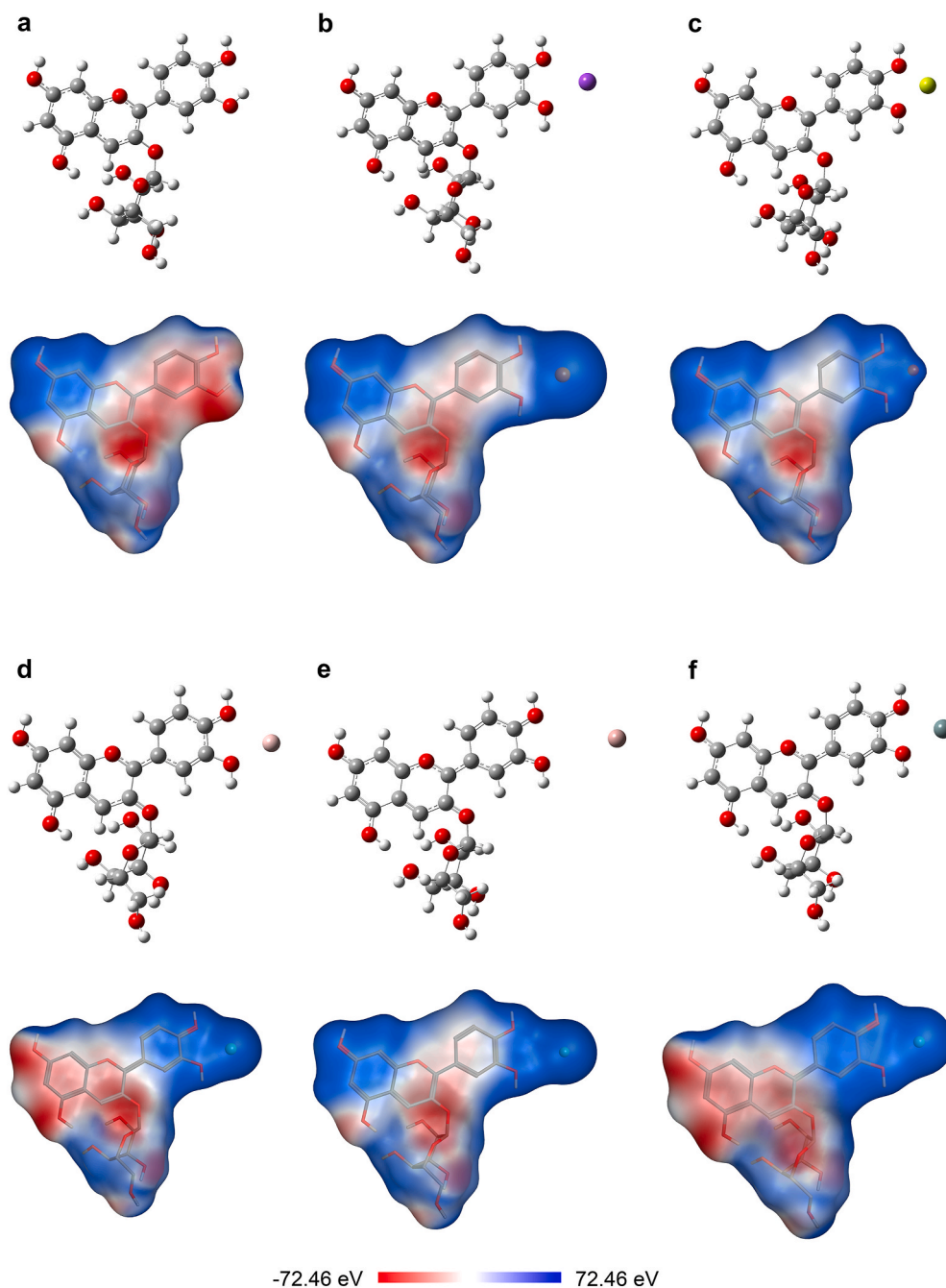[b] Hartree = 2625.50 kJ/mol.

Fig. 3. The optimized geometries and charge density diagrams of C3OG (a) and its complexes with five metal ions (b, K^+/C3OG; c, Mg^{2+}/C3OG; d, Al^{3+}/C3OG; e, Ga^{3+}/C3OG; f, Sn^{4+}/C3OG).

lifetime τave of 116.0 ps. Upon binding with Mg^{2+}, the average lifetime of the Mg^{2+}/C3OG complex was significantly reduced to 87.2 ps (Fig. 4h and Table S3), indicating a clear occurrence of electron transfer from anthocyanin to Mg^{2+}. The influence exerted by higher valent metal ions was even more pronounced, as evidenced by the average lifetime reduction to 7.3 ps for the Sn^{4+}/C3OG complex (Fig. 4i and Table S3).

In addition to the TA spectra for other complexes in Fig. S1, we overlapped the dynamic curves in Fig. S2. Based on these data, two conclusions can be drawn. Firstly, electron transfer occurred from anthocyanin to metal ions after complexation, as evidenced by a decrease in average lifetime compared with pristine anthocyanin. Secondly, the decreasing order of complex lifetimes was found to be K^+, Mg^{2+}, Al^{3+}, Ga^{3+} and Sn^{4+} (from lowest to highest valency), which is consistent with steady-state absorption measurements and color

analysis. The calculated electron transfer rates (k) from anthocyanin to metal ions were $2.9 \times$, $3.7 \times$, $5.8 \times$, $75.4 \times$ and $128.4 \times 10^9 \, s^{-1}$ for K^+, Mg^{2+}, Al^{3+}, Ga^{3+}, and Sn^{4+} complexes respectively using the equation $k = 1/\tau - 1/\tau_0$. Clearly, higher-valent ion complexes demonstrated higher electron transfer rates.

3.5. Frontier molecular orbitals analysis

The frontier molecular orbitals (FMOs) depicted in Fig. 5 are presented to investigate further the charge distribution and charge transfer behaviors of metal/C3OG complexes. The most crucial FMOs, namely the highest occupied molecular orbital (HOMO) and the lowest unoccupied molecular orbital (LUMO) govern a molecule's capabilities in electron gain, loss, and transfer. Therefore, these FMOs play a pivotal
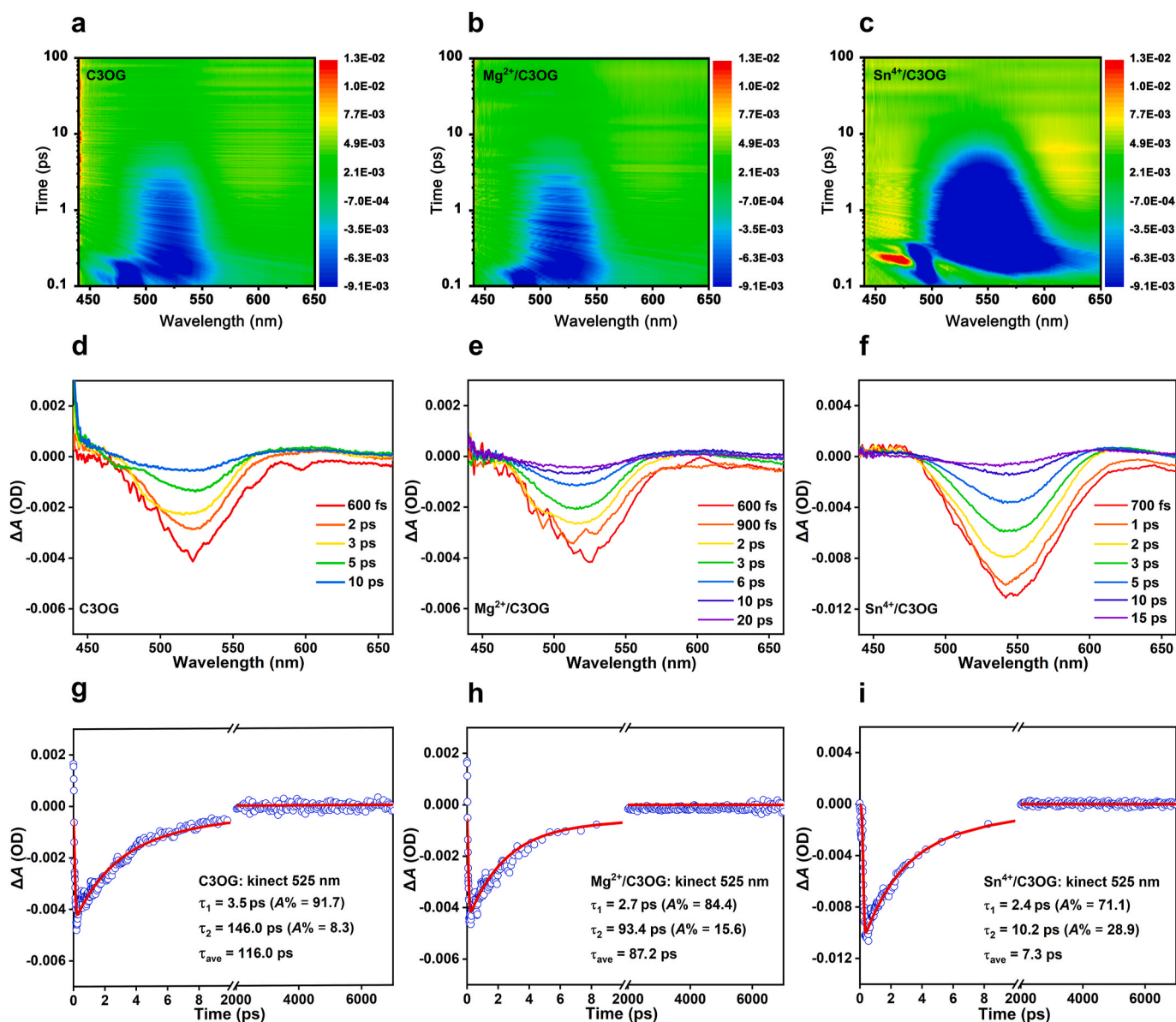
Fig. 4. Contour maps of transient absorption spectra of C3OG (a), Mg^{2+}/C3OG (b), and Sn^{4+}/C3OG (c) excited at 420 nm; Representative spectra at different delay times for C3OG (d), Mg^{2+}/C3OG (e), and Sn^{4+}/C3OG (f); The kinetic traces of C3OG (g), Mg^{2+}/C3OG (h), and Sn^{4+}/C3OG (i) at 525 nm.

role in determining a molecule's chemical stability and interatomic interactions within it (Lohith et al., 2022).

As illustrated in Fig. 5, the FMOs are predominantly localized between the B ring of C3OG and the cation. The electron transition from HOMO to LUMO primarily involves the transfer of electrons from the hydroxyl group located at position B ring of C3OG to the cation, resulting in a modification of electron density within the B ring of C3OG and an adjustment of electron density within both the C ring and A ring. A similar phenomenon has also been observed in Milenkovic's research, where it was found that aromatic rings can induce the formation of a ring current system by conjugation effects (Milenković et al., 2018). This process facilitates hydrogen proton or proton-coupled electron transfer and promotes substance interactions. By calculating the energy difference (ΔE) between HOMO and LUMO, we observed a strong correlation between the magnitude of ΔE and the valence state of the metal ion. The smallest ΔE value was found for tetravalent Sn^{4+} (1.466 eV), followed by Ga^{3+} (1.675 eV), Al^{3+} (1.780 eV), Mg^{2+} (1.895 eV) and K^+ (2.146 eV), as shown in Fig. 5. In general, a smaller energy gap between orbitals indicates increased ease of electron excitation, heightened chemical

reactivity, softness, as well as enhanced instability (Janeoo et al., 2022). Consequently, this leads to an extended maximum wavelength and a more pronounced bathochromic shift in the molecule's absorption spectrum. Furthermore, the reduced energy difference facilitates electron transition with higher probability and intensifies the hyperchromic effect by promoting electron transfer processes (Zhang, 2015). This result aligns with visible absorption spectra findings that highlight the crucial role played by metal ion-induced electron transfer in driving copigmentation processes.

4. Conclusions

In this study, five metal ions (K^+, Mg^{2+}, Al^{3+}, Ga^{3+}, and Sn^{4+}) detected in common fruits were utilized as copigments to investigate their copigmentation processes with C3OG in simulated fruit wine solutions. The color characteristics were analyzed using the Glories and CIELAB methods. The copigmentation effects and color characteristics exhibited a strong dependence on the concentration of cations, resulting in darker and more vivid red-blue hues. Furthermore, higher valence
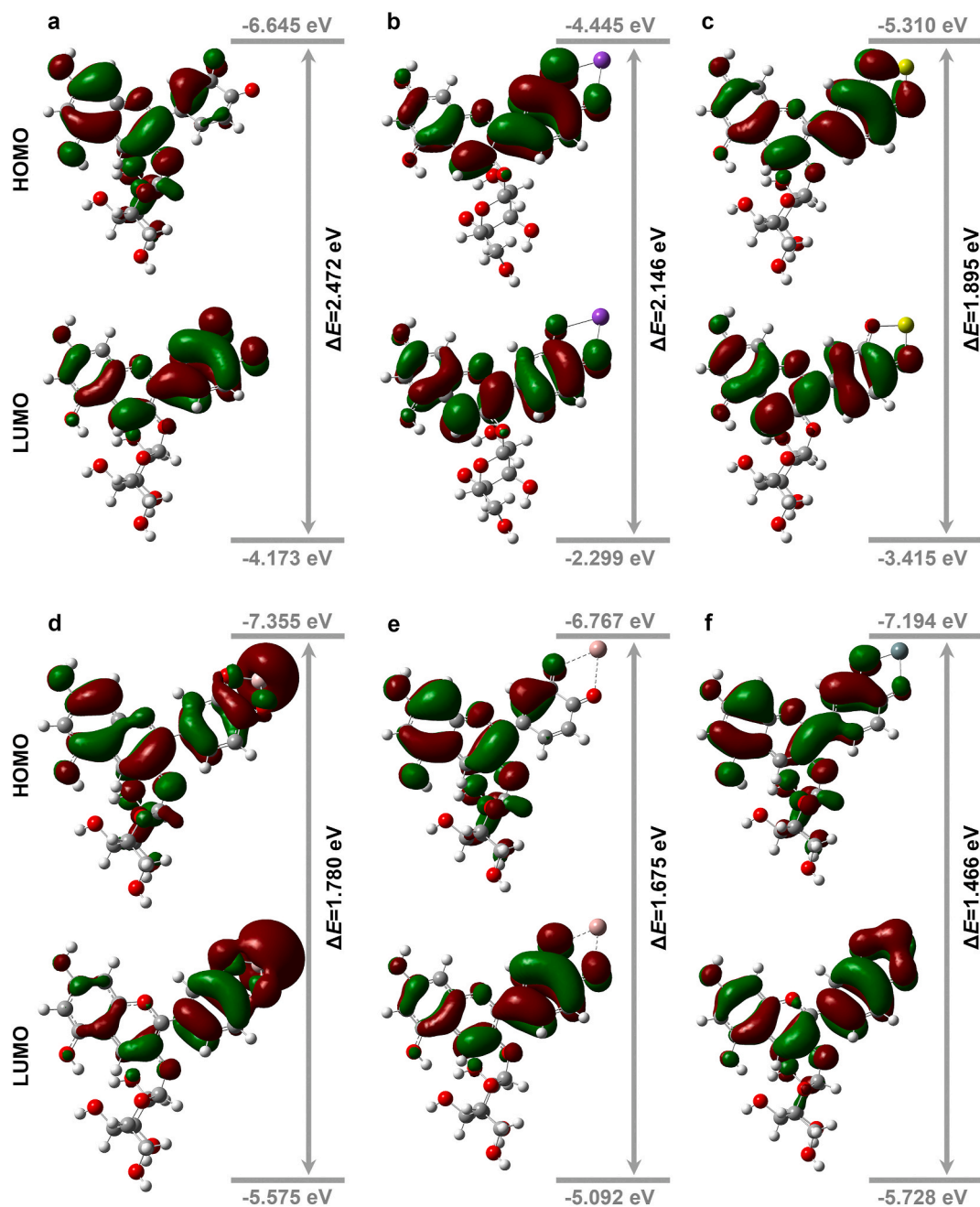
Fig. 5. HOMO and LUMO orbitals of C3OG (a), K^+/C3OG (b), Mg^{2+}/C3OG (c), Al^{3+}/C3OG (d), Ga^{3+}/C3OG (e), and Sn^{4+}/C3OG (f).

states of cations favored copigmentation, following the trend Sn^{4+} $>Ga^{3+} > Al^{3+} > Mg^{2+} > K^+$. Thermodynamic analysis revealed that the interaction between metal cations and C3OG was a spontaneous exothermic reaction, except for K^+, which exhibited lower effectiveness. The K indicated that the combination of metal ions and C3OG was influenced by their valence state, ionic radii and electronegativity, suggesting electron transfer between reactants. The photoinduced electron transfer process between cations and C3OG was monitored in situ using ultra-fast femtosecond spectroscopy, revealing that electron transfer occurred from anthocyanin to the metal ions. Moreover, it was observed that the efficiency of this electron transfer is contingent upon the valence state of cations. This investigation provides valuable insights into understanding the dynamic copigmentation mechanism. Furthermore, analysis based on HOMO-LUMO data validates that cations with higher valence demonstrate enhanced efficacy in facilitating electron transfers, underscoring the pivotal role played by metal ion-induced

processes in driving copigmentation. These findings would contribute to a deeper comprehension of the involvement of cations in pigment/metal complexes and color chemistry, thereby expanding the theoretical framework for copigmentation and broadening its potential applications in natural color enhancement within the beverage industry.

Funding

02Y06].

CRediT authorship contribution statement

Bo Zhang: Conceptualization, Data curation, Supervision, Writing – original draft. **Juan-Di Wu:** Investigation, Visualization. **Qiang Wang:** Writing – review & editing. **Shu-Yan Wang:** Investigation, Visualization. **Pan-Pan Zhou:** Software, Investigation, Validation. **Li-Ting Han:** Investigation.

Declaration of competing interest

The authors declare that they have no known competing financial interests or personal relationships that could have appeared to influence the work reported in this paper.

Data availability

Data will be made available on request.

Acknowledgments

We acknowledge all people for their efforts in this study.

Appendix A. Supplementary data

Supplementary data to this article can be found online at https://doi.org/10.1016/j.crfs.2024.100849.

References

Bingol, A., Turkyilmaz, M., Ozkan, M., 2022. Increase in thermal stability of strawberry anthocyanins with amino acid copigmentation. Food Chem. 384, 132518 https://doi.org/10.1016/j.foodchem.2022.132518.

Boulton, R., 2001. The copigmentation of anthocyanins and its role in the color of red wine: a critical review. Am. J. Enol. Vitic. 52 (2), 67–87. https://doi.org/10.5344/ajev.2001.52.2.67.

Chen, M., Luo, D., Yang, Y., Lahaye, M., Tang, T., Lan, W., Liu, Y., 2024. Exploring the impact of co-extracted cell wall polysaccharides on the stability of blueberry anthocyanins in deep eutectic solvent. Chem. Eng. J. 494, 153065 https://doi.org/10.1016/j.cej.2024.153065.

Cortez, R., Luna-Vital, D.A., Margulis, D., Gonzalez de Mejia, E., 2017. Natural pigments: stabilization methods of anthocyanins for food applications. Compr. Rev. Food Sci. Food Saf. 16 (1), 180–198. https://doi.org/10.1111/1541-4337.12244.

Czibulya, Z., Horváth, I., Kollár, L., Nikfardjam, M.P., Kunsági-Máté, S., 2015. The effect of temperature, pH, and ionic strength on color stability of red wine. Tetrahedron 71 (20), 3027–3031. https://doi.org/10.1016/j.tet.2015.01.036.

Estévez, L., Otero, N., Mosquera, R.A., 2010. Molecular structure of cyanidin metal complexes: Al(III) versus Mg(II). Theor. Chem. Acc. 128 (4–6), 485–495. https://doi.org/10.1007/s00214-010-0829-0.

Falamas, A., Tosa, N., Tosa, V., 2017. Measuring the frequency chirp of white-light continuum in a pump-probe system. J. Optoelectron. Adv. Mater. 19 (5–6), 291–297.

Fedenko, V.S., Shemet, S.A., Landi, M., 2017. UV-vis spectroscopy and colorimetric models for detecting anthocyanin-metal complexes in plants: an overview of *in vitro* and *in vivo* techniques. J. Plant Physiol. 212, 13–28. https://doi.org/10.1016/j.jplph.2017.02.001.

Ferreira da Silva, P., Lima, J.C., Freitas, A.A., Shimizu, K., Maçanita, A.L., Quina, F.H., 2005. Charge-transfer complexation as a general phenomenon in the copigmentation of anthocyanins. J. Phys. Chem. A 109 (32), 7329–7338. https://doi.org/10.1021/jp052106s.

Gal, A.W., 2011. Metal-organic Chemistry. Encyclopedia of Inorganic and Bioinorganic Chemistry.

Gokilamani, N., Muthukumarasamy, N., Thambidurai, M., Ranjitha, A., Velauthapillai, D., 2014. Grape pigment (malvidin-3-fructoside) as natural sensitizer for dye-sensitized solar cells. Materials for Renewable and Sustainable Energy 3, 33. https://doi.org/10.1007/s40243-014-0033-6.

Huang, Y., Zhou, S., Zhao, G., Ye, F., 2021. Destabilisation and stabilisation of anthocyanins in purple-fleshed sweet potatoes: a review. Trends Food Sci. Technol. 116, 1141–1154. https://doi.org/10.1016/j.tifs.2021.09.013.

Janeoo, S., Reenu, Saroa, A., Kumar, R., Kaur, H., 2022. Computational investigation of bioactive 2,3-diaryl quinolines using DFT method: FT-IR, NMR spectra, NBO, NLO, HOMO-LUMO transitions, and quantum-chemical properties. J. Mol. Struct. 1253, 132285 https://doi.org/10.1016/j.molstruc.2021.132285.

Kuang, L., Wang, Z., Zhang, J., Li, H., Xu, G., Li, J., 2022. Factor analysis and cluster analysis of mineral elements contents in different blueberry cultivars. J. Food Compos. Anal. 109, 104507 https://doi.org/10.1016/j.jfca.2022.104507.

Kunsági-Máté, S., Stampel, E., Kollár, L., Nikfardjam, M.S.P., 2008. The effect of the oxidation state of iron ions on the competitive complexation of malvidin by caffeic or ellagic acid. Food Res. Int. 41 (7), 693–696. https://doi.org/10.1016/j.foodres.2008.05.001.

Li, B.R., 2020. Structural Chemistry. Higher Education Press. Beijing (China).

Li, X.D., Li, J., Wang, M., Jiang, H., 2016. Copigmentation and thermal degradation kinetics of purple sweet potato anthocyanins with metal ions and sugars. Applied Biological Chemistry 59 (1), 15–24. https://doi.org/10.1007/s13765-015-0140-9.

Lohith, T.N., Hema, M.K., Karthik, C.S., Sandeep, S., Mallesha, L., Alsaiari, N.S., Kumaraswamy, S.R., 2022. Persistent prevalence of non-covalent interaction in pyrimidine containing sulfonamide derivative: a quantum computational analysis. J. Mol. Struct. 1266, 133378 https://doi.org/10.1016/j.molstruc.2022.133378.

Lv, X., Li, L., Lu, X., Wang, W., Sun, J., Liu, Y., Wang, J., 2022. Effects of organic acids on color intensification, thermodynamics, and copigmentation interactions with anthocyanins. Food Chem. 396, 133691 https://doi.org/10.1016/j.foodchem.2022.133691.

Malaj, N., De Simone, B.C., Quartarolo, A.D., Russo, N., 2013. Spectrophotometric study of the copigmentation of malvidin 3-*O*-glucoside with *p*-coumaric, vanillic and syringic acids. Food Chem. 141 (4), 3614–3620. https://doi.org/10.1016/j.foodchem.2013.06.017.

Martínez, J.A., Melgosa, M., Pérez, M.M., Hita, E., Negueruela, A.I., 2001. Note. Visual and instrumental color evaluation in red wines. Food Sci. Technol. Int. 7 (5), 439–444. https://doi.org/10.1106/VFAT-5REN-1WK2-5JGQ.

Milenković, D., Đorović, J., Petrović, V., Avdović, E., Marković, Z., 2018. Hydrogen atom transfer versus proton coupled electron transfer mechanism of gallic acid with different peroxy radicals. React. Kinet. Mech. Catal. 123 (1), 215–230. https://doi.org/10.1007/s11144-017-1286-8.

Pérez-Magariño, S., González-San José, M.L., 2002. Prediction of red and rosé wine CIELab parameters from simple absorbance measurements. J. Sci. Food Agric. 82 (11), 1319–1324. https://doi.org/10.1002/jsfa.1191.

Schreiber, H.D., Swink, A.M., Godsey, T.D., 2010. The chemical mechanism for Al³⁺ complexing with delphinidin: a model for the bluing of hydrangea sepals. J. Inorg. Biochem. 104 (7), 732–739. https://doi.org/10.1016/j.jinorgbio.2010.03.006.

Shen, Huan, Lin-Qiang, Hua, Zheng-Rong, W., 2022. Solvent effect on ultrafast decay of uracil studied by femtosecond transient absorption spectroscopy. Acta Phys. Sin. 71 (18), 184206 https://doi.org/10.7498/aps.71.20220515.

Shimizu, H., Akamatsu, F., Kamada, A., Koyama, K., Iwashita, K., Goto-Yamamoto, N., 2022. Effects of variety and vintage on the minerals of grape juice from a single vineyard. J. Food Compos. Anal. 107, 104377 https://doi.org/10.1016/j.jfca.2021.104377.

Shiono, M., Matsugaki, N., Takeda, K., 2005. Structure of the blue cornflower pigment. Nature 436 (7052), 791. https://doi.org/10.1038/436791a, 791.

Sigurdson, G.T., Robbins, R.J., Collins, T.M., Giusti, M.M., 2017. Effects of hydroxycinnamic acids on blue color expression of cyanidin derivatives and their metal chelates. Food Chem. 234, 131–138. https://doi.org/10.1016/j.foodchem.2017.04.127.

Squadrone, S., Brizio, P., Stella, C., Mantia, M., Pederiva, S., Giordanengo, G., Abete, M.C., 2020. Distribution and bioaccumulation of trace elements and lanthanides in apples from Northwestern Italy. J. Trace Elem. Med. Biol. 62, 126646 https://doi.org/10.1016/j.jtemb.2020.126646.

Strassfeld, D.A., Chen, C.Y., Park, H.S., Phan, D.Q., Yu, J.Q., 2023. Hydrogen-bond-acceptor ligands enable distal C(*sp3*)–H arylation of free alcohols. Nature 622 (7981), 80–86. https://doi.org/10.1038/s41586-023-06485-8.

Tang, R., He, Y., Fan, K., 2023. Recent advances in stability improvement of anthocyanins by efficient methods and its application in food intelligent packaging: A review. Food Bioscience 56, 103164. https://doi.org/10.1016/j.fbio.2023.103164.

Trouillas, P., Sancho-Garcia, J.C., De Freitas, V., Gierschner, J., Otyepka, M., Dangles, O., 2016. Stabilizing and modulating color by copigmentation: Insights from theory and experiment. Chem. Rev. 116 (9), 4937–4982. https://doi.org/10.1021/acs.chemrev.5b00507.

Ujihara, T., Hayashi, N., 2020. Mechanism of copigmentation of monoglucosylrutin with caffeine. J. Agric. Food Chem. 68 (1), 323–331. https://doi.org/10.1021/acs.jafc.9b06235.

Vaňura, P., Sýkora, D., Uhlíková, T., 2022. Reaction of the thallium(I) cation with [2.2] paracyclophane: experimental and theoretical study. Inorg. Chim. Acta. 543, 121205 https://doi.org/10.1016/j.ica.2022.121205.

Wang, Y., Zhao, Y., Sun, B., Yang, Y., Wang, S., Feng, Z., Li, J., 2024. The structure of anthocyanins and the copigmentation by common micromolecular copigments: a review. Food Res. Int. 176, 113837 https://doi.org/10.1016/j.foodres.2023.113837.

Wardani, N.I., Alahmad, W., Varanusupakul, P., 2024. A review of utilizing anthocyanins as natural reagents for eco-friendly solid-state colorimetric sensors: a green perspective. Green Analytical Chemistry 9, 100117. https://doi.org/10.1016/j.greeac.2024.100117.

Yang, H., Cai, G., Lu, J., Gómez Plaza, E., 2021. The production and application of enzymes related to the quality of fruit wine. Crit. Rev. Food Sci. Nutr. 61 (10), 1605–1615. https://doi.org/10.1080/10408398.2020.1763251.

Zeece, M., 2020. Chapter eight - food colorants. In: Zeece, M. (Ed.), Introduction to the Chemistry of Food. Academic Press, pp. 313–344.

Zhai, X.P., Ma, B., Wang, Q., Zhang, H.L., 2020. 2D materials towards ultrafast photonic applications. Phys. Chem. Chem. Phys. 22 (39), 22140–22156. https://doi.org/10.1039/D0CP02841J.

Zhang, B., He, F., Zhou, P.P., Liu, Y., Duan, C.Q., 2016. The color expression of copigmentation between malvidin-3-*O*-glucoside and three phenolic aldehydes in

model solutions: the effects of pH and molar ratio. Food Chem. 199, 220–228. https://doi.org/10.1016/j.foodchem.2015.12.008.

Zhang, B., Wang, Q., Zhou, P.P., Li, N.N., Han, S.Y., 2020. Copigmentation evidence of oenin with phenolic compounds: a comparative study of spectrographic, thermodynamic and theoretical data. Food Chem. 313, 126163 https://doi.org/10.1016/j.foodchem.2020.126163.

Zhang, B., Wang, X.Q., Yang, B., Li, N.N., Niu, J.M., Shi, X., Han, S.Y., 2021. Copigmentation evidence of phenolic compound: the effect of caffeic and rosmarinic acids addition on the chromatic quality and phenolic composition of Cabernet Sauvignon red wine from the Hexi Corridor region (China). J. Food Compos. Anal. 102, 104037 https://doi.org/10.1016/j.jfca.2021.104037.

Zhang, H., 2015. *Spectroscopic Identification Of Organic Structure.* Dalian (Chian). Dalian University of Technology Press.

Zhang, J., Zhu, B., Zhang, L., Yu, J., 2023. Femtosecond transient absorption spectroscopy investigation into the electron transfer mechanism in photocatalysis. Chem. Commun. 59 (6), 688–699. https://doi.org/10.1039/D2CC06300J.

Zhang, S.H., Liu, L.Y., Ma, Y.Q., Di, C.A., 2024. Advances in theoretical calculations of organic thermoelectric materials. Chin. Chem. Lett. 35 (8), 109749 https://doi.org/10.1016/j.cclet.2024.109749.

Zhao, X., Ding, B.W., Qin, J.W., He, F., Duan, C.Q., 2020. Intermolecular copigmentation between five common 3-O-monoglucosidic anthocyanins and three phenolics in red wine model solutions: the influence of substituent pattern of anthocyanin B ring. Food Chem. 326, 126960 https://doi.org/10.1016/j.foodchem.2020.126960.